L-PBF processing and characterization of a Ti 35 Nb 30 Zr 29 Mo 3 Ta 3 multiprincipal element alloy for medical implants

Farzin Arjmand, Adrien Mourgout, Alima Chali, Madjid Djemai, Credson-Yannick Langueh, Olivier Monasson, Elisa Peroni, Michel Boissière, Souad Ammar, Guy Dirras

L-PBF processing and characterization of a $Ti_{35}Nb_{30}Zr_{29}Mo_3Ta_3$ multiprincipal element alloy for medical implants

Farzin Arjmand,[1*] Adrien Mourgout,[2] Alima Chali,[1] Madjid Djemai,[3] Credson-Yannick Langueh,[4] Olivier Monasson,[5,6] Elisa Peroni,[5,6] Michel Boissiere,[4] Souad Ammar,[1] Guy Dirras[2]

[1] Université Paris Cité, CNRS UR 7086, ITODYS, 75205 Paris, France
[2] Université Sorbonne Paris Nord, CNRS UPR 3407, LSPM, 93430 Villetaneuse, France
[3] Z3DLAB sas, 95270 Chaumontel, France
[4] CY Cergy Paris Université, ERRMECe, 95000 Cergy Pontoise, France
[5] CY Cergy Paris Université, CNRS, BioCIS, 95000 Cergy Pontoise, France
[6] Université Paris-Saclay, CNRS, BioCIS, 92290 Châtenay-Malabry, France

[*]Corresponding author E-mail address: farzin.arjmand@gmail.com

ABSTRACT

This letter reports on the processing, mechanical properties, electrochemical performance and toxicity behavior of a multiprincipal element $Ti_{35}Nb_{30}Zr_{29}Mo_3Ta_3$ alloy. The recovered centimeter-sized cubes or parallelepipeds were polished before analysis. It was found that the homogeneity and yield stress of the alloys get increased when higher volumetric energy densities (VEDs) are applied during processing. The synthesized alloys also exhibited a Young modulus closer to those of bones than those usually reported on the conventional orthopedic metals (60-80 GPa for this alloy against 110 and 4-30 GPa for the Ti-6Al-4V and bone, respectively). The electrochemical corrosion assays performed at 25°C and 37°C, in sodium chloride (NaCl, 0.1 M), deoxygenated high glucose Dulbecco's Modified Eagle Medium (DMEM) and deoxygenated DMEM implemented with Fetal Bovine Serum (FBS) showed corrosion potentials (E_{corr}) ranged in the order $NaCl_{(25°C)} \approx DMEM + PBS_{(37°C)} > DMEM_{(37°C)}$, and impedances much larger in the DMEM and DMEM + PBS media than in NaCl. Finally, pre-osteoblasts cells cultured in the medium conditioned by the alloy did not evidence cytotoxicity effect, because no effects on the cell proliferation and morphology were observed. These data suggest the biocompatibility of this alloy, indicating no acute toxicity, which is a prerequisite for the integration of an alloy as a bioimplant.

Faced with the aging population in our modern societies and the increased risk of bone diseases and accidents in these populations, the development of long-lasting implant materials is a significant

public health issue. It is, nowadays, essential to adapt advanced structural materials to extend the net duration of the revision surgery beyond the current limit of ten years.[1] According to the recent United Nations reports, the over 60s population of the world is growing, and the proportion of the old persons is expected to increase by 45% by 2050, with a life expectancy that could gain another five additional years in the developed countries,[2] making this period of ten years before the surgical revision extremely short. The problem of the longer-lasting implants also concerns people with acute and chronic bone diseases while maintaining an acceptable perspective and quality of life.

Multiprincipal element alloys (MPEAs) are a new class of materials that offer a range of unique properties, such as high strength and corrosion resistance.[3,4] These properties make them ideal candidates for designing medical devices. Moreover, by adjusting the composition of the MPEAs, it is possible to create materials that are optimized for specific applications. For instance, their Young's modulus can be reduced to values close to those of bones (20 to 30 GPa), without losing their yield strength, thereby reducing the probability of the occurrence of osteoporosis near the implant. Consequently, the MPEAs are increasingly being used in the medical industry for various applications.[5]

In parallel, the emergence of the additive manufacturing (AM) has revolutionized the production of complex and intricate structures, previously impossible to be manufactured[6]; opening thus real opportunities for medical implant processing, meaning that AM allows the production of medical implants tailored to the patient's needs, matching correctly the targeted function.

The technology behind the AM is based on the principles of the layer-by-layer deposition of materials. This means that the implant is built up from a series of thin layers, and each layer is deposited on top of the previous one. In this way, the AM eliminates the need for the expensive and time-consuming tooling. It also enables the production of porous structures, which can serve as channels for drug storage and then controlled delivery,[7] as it allows surface texturing, which can be useful for tissue integration and rejection risk reduction.[8]

Altogether, the AM designed MPEAs-based biomedical implants have the potential to revolutionize healthcare.[9] Combining these two innovative concepts, the implants composition and morphology

would be easily tailored to meet patients' anatomy, age, and gender, laying the ground for personalized treatment.

In this study, a series of the MPEA with the nominal composition of $Ti_{39}Nb_{28}Zr_{28}Mo_{2.5}Ta_{2.5}$ (at. %) were elaborated by the laser powder bed fusion (L-PBF), using the selected laser melting (SLM) technology (see Table 1S for the actual achieved composition). By adjusting the fabrication parameters, especially the volumetric energy density (VED) during the SLM processing, the Young's modulus of the alloy was significantly reduced, without losing its yield strength, reducing thereby the probability of osteoporosis occurrence near the implant.

Through the processing optimization, several types of microstructural defects were identified (experimental details in the supplementary data). These were mainly unmelted powders, cracks, and pits.

Melting elements like Ta, Mo and Nb with high melting points (3020, 2623 and 2477°C, respectively) is obviously arduous. The low VED resulted in the accumulation of unmelted Nb/Mo/Ta-rich islands. Scanning electron microscopy (SEM) images clearly evidence these entities by their after polishing relief and light grey contrast (as well as the Ta/Ta-rich islands by their bright light contrast), as shown in Figs. 1(a) and 1S.

Increasing the VED induced the Nb/Mo/Ta-rich islands solubilization, improving the homogeneity of the final alloy (Fig. 1(b, c)). Nevertheless, the solubilization of Nb/Mo/Ta into the matrix triggers the vaporization of Ti, since the melting point of Ta is close to the boiling point of Ti (3287°C). As a consequence, typical processing defects, such as keyhole porosities form. The higher the VED, the higher the keyhole porosities fraction was in the structure of the alloy. Their appearance frequency, means the coalescence of the cavities while porosities facilitate the degradation of the mechanical properties of the alloy.[12] Contrariwise, cracks cause less dramatic effects on the mechanical properties of the material. Cracking occurs either as a result of the residual stress relaxations (induced by the high cooling rate of the SLM) or the complex solidification mechanisms (involving the solidification range and liquid viscosity) (Fig. 1(e, f)). The second case usually forms short/thin intergranular cracks, primarily along the high-angle grain boundaries (HAGBs).

The VED affects also the grain morphology, size and size distribution. The inverse pole figure (IPF) electron backscatter diffraction (EBSD) images recorded on the specimens, elaborated at the VED = 150, 450, and 550 J.mm^{-3}, clearly evidence it (Fig. 2(a-c)). These images show heterogeneous grain shapes. The degree of heterogeneity decreases with the applied VED. For the VED = 550 J.mm^{-3}, a relatively bimodal character was observed, while for the VED = 450 J.mm^{-3}, a slight <100> texture was noted.

On a finer scale, the grains appeared as made up of dendritic cells whose sizes increased with increasing the VED, from 429 up to 516, and 740 nm, for the VED = 150, 450 and 550 J.mm^{-3}, respectively (Fig. 2(d-f)). The statistical details of the microstructure of the alloys can be seen in Fig. 2(g, h). These observations are in agreement with the existing literature data,[10,11] where it has been reported that the walls between the cells are made of accumulated geometrically necessary dislocations, inducing the disorientations in the order of 2 degrees. Furthermore, the dendritic cell walls were rich in Zr, while Mo was accumulated mostly inside the cells (Fig. 2S).

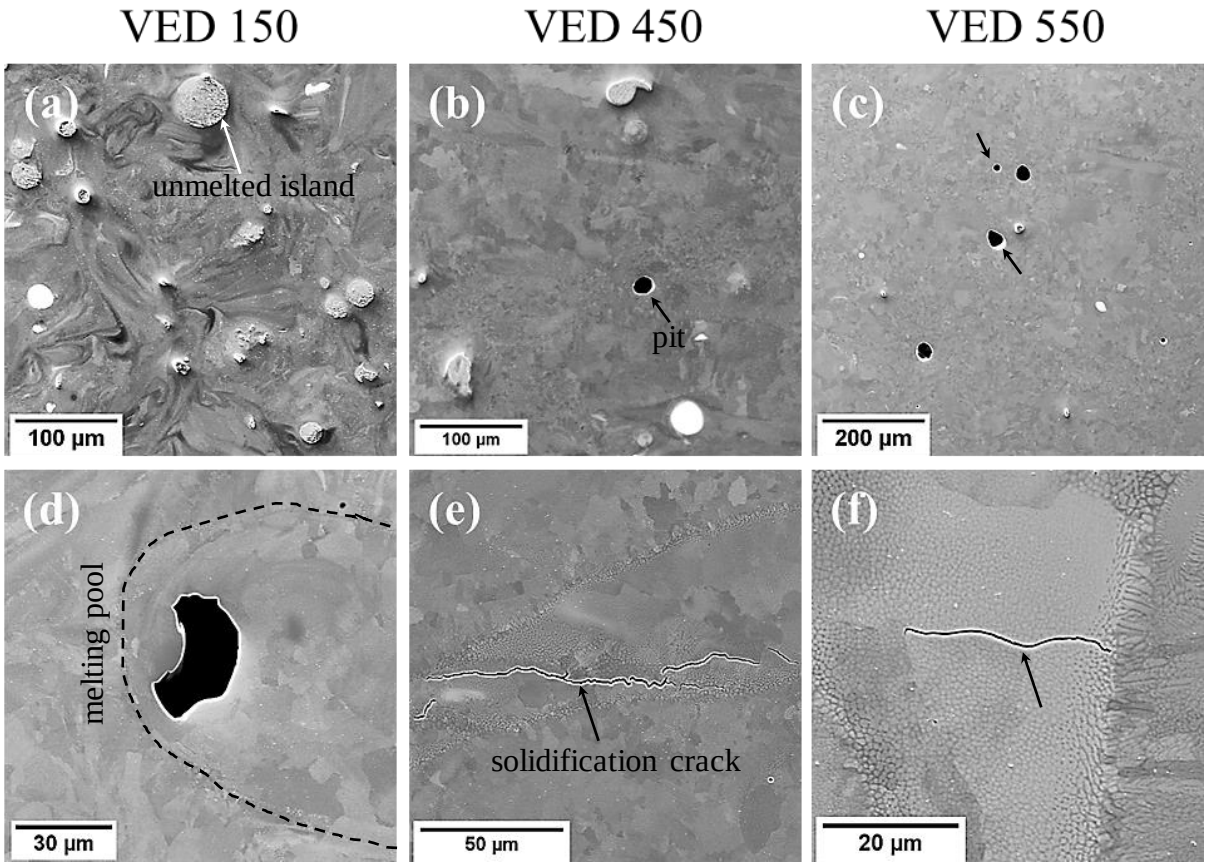

FIG. 1. Nature of the processing defects observed as a function of the applied VED. (a, d) 150 J.mm^{-3}, (b, e) 450 J.mm^{-3} and (c , f) 550 J.mm^{-3}.

The number of the HAGBs increased with increasing the VED. The average degrees of misorientations were 24, 28, and 32° for the VED = 150, 450, and 550 J.mm^{-3}, respectively (Fig. 2(g)). The high fraction of low angle grain boundary (LAGB) misorientation at low VED is in line with the cells size given in Fig. 2(h). Indeed, smaller cell sizes (longer cell walls) increased the degree of the low angle misorientation. The increase in the HAGBs' percentage coincided with the solidification cracking probably due to the increase in the disorientation between the contiguous grains, in agreement with the literature data.[12]

Apart from the evolution of the size of the dendritic cells which increased with the VED (Fig. 2(d-f)), the average grain size of the alloys (measured as area fraction) decreased as the VED increased. The latter is attributed to the bimodality of the alloy structure (Fig. 2(a-c)).

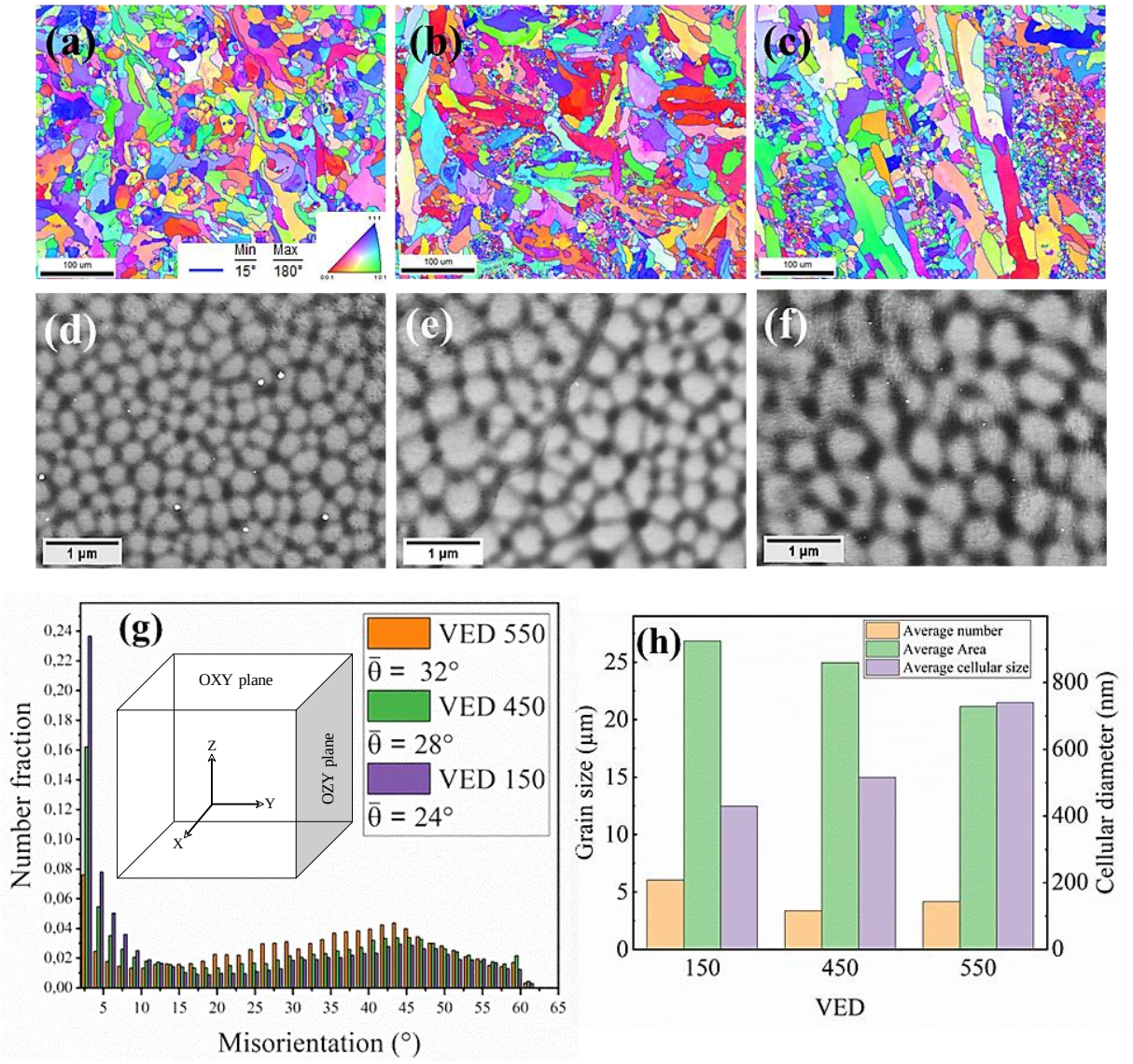

FIG. 2. Microstructure quantification details. (a-c) IP EBSD images superimposed to the grain boundaries map of the VED = 150, 450 and 550 J.mm^{-3} specimens, respectively, (d-f) SEM images of the cellular substructure of each specimen and (g, h) distribution of the misorientation across the grain boundaries, frequency of grain, and cellular size as a function of the applied VED (Z axis in Fig (g) indicates the laser beam direction).

The results of the compression and tension tests can be compared in Fig. 3(a, b). See also experimental details in the supplementary data. Fig. 3(a) depicts that all the as-processed alloys possess a high ability to get plastically deformed. Indeed, all the specimens exhibited nominal strains well above 70%. The yield stresses were found to be in the range from 900 to 1350 MPa, increasing with the VED increase. As expected, the above-mentioned processing defects did not compromise the use of these alloys in the loading conditions. Contrariwise, the tensile tests showed a high sensitivity to the microstructure. The higher the VED, the higher were the yield stress and yield strength values. For

instance, the VED = 550 J.mm^{-3} led to a relatively poor ductility. The related specimen is in the regime with the highest keyhole porosities frequency, along with the solidification cracking. The coalescence of these cavities during the straining and bridging of the microcracks into a three-dimensional network, contributed to the observation of the lack of ductility. Fig. 3(c, d) illustrates the necking regions of the 550 and 450 J.mm^{-3} specimens, respectively. The elongation of the Ta-rich entities into a lenticular shape in the latter is evident; since opposite to the 550 J.mm^{-3} specimen, here they contributed to the overall ductility of the material. Images of the generated microcracks in the 450 J.mm^{-3} specimen are also given in Fig. 3(d, e).

Here the increase in the yield strength by increasing the VED can be explained by a Hall-Petch-like effect combined with a solid solution strengthening. The Hall-Petch-like effect comes from the reduction of the grain size while the origin of the solid solution strengthening comes from the solubilization of Nb/Mo/Ta in the matrix.

Table 1 summarizes the major compression and tensile loading parameters of the alloys. Here the Young's modulus E values (60 to 80 GPa) are much lower than those of the materials that are currently used for the orthopedic applications (CP-Ti: 105, Ti-6Al-4V: 115 and Co-Cr: 240 GPa). The low E values are expected to eliminate the stress shielding effect of the material.[13,14] Another biomechanical indicator for the metallic implant materials, is the elastic strain deformation ε.[15] It was computed, for this study, from the tensile test data as $\varepsilon = \sigma_{YS}/E$. The obtained values were found to be varying in the range from 0.87 to 1.22%, larger than those of the CP-Ti and Ti6Al4V (0.47 and 0.78%, respectively), but closer to that of the as-cast TiZrNbTa (1.26%).[16]

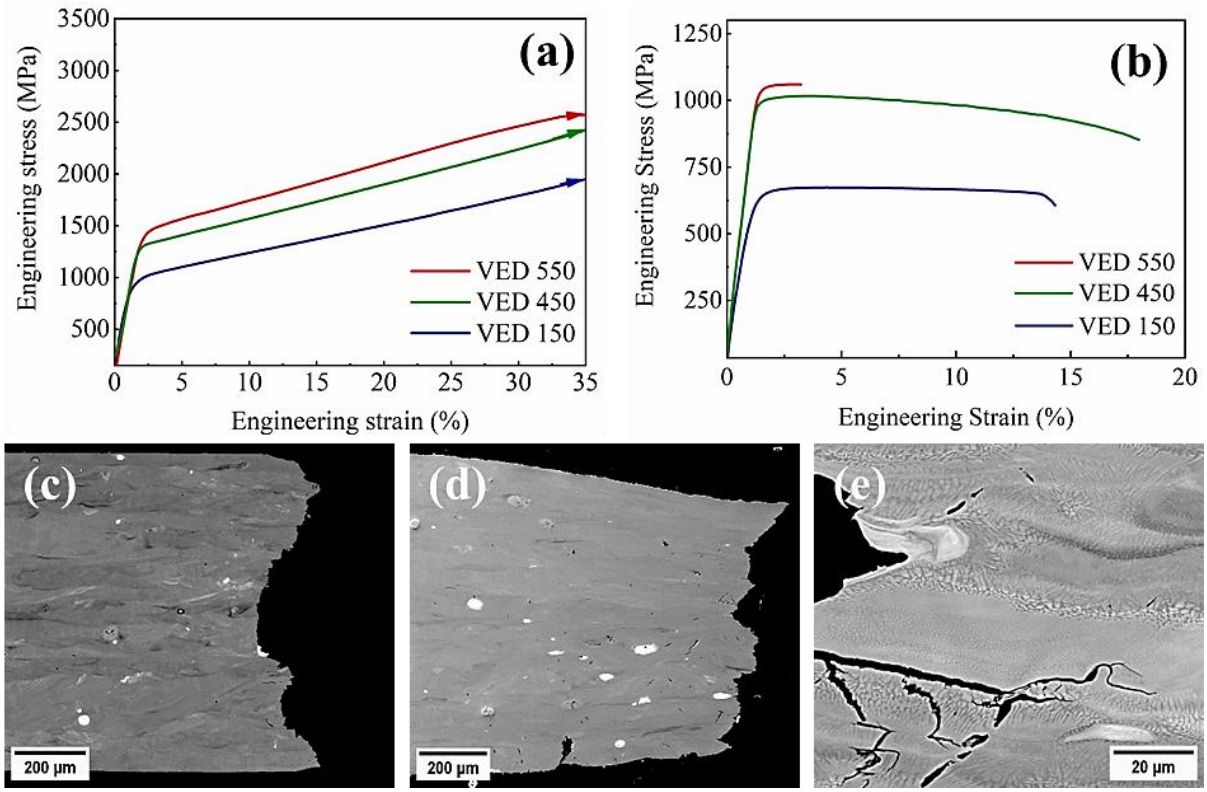

FIG. 3. (a) Typical stress-strain compression test plots of the synthesized alloys along the Z axis/OXY plane (building direction), (b) tensile test plots along the OYZ plane, (c, d) failure profiles of the tensile tested 550 and 450 J.mm^{-3} specimens, respectively and (e) crack propagation along the HAGBs in the tensile tested 450 J.mm^{-3} specimen.

Table 1. Some mechanical parameters of the 150, 450 and 550 J.mm^{-3} specimens.

specimen	Young modulus [GPa]	ultimate tensile stress [MPa]	yield strength [MPa]	strain to failure [%]	compression yield strength (MPa)
VED = 150 J.mm^{-3}	60	674	527	13.38	940
VED = 450 J.mm^{-3}	78	1016	950	17.99	1215
VED = 550 J.mm^{-3}	80	1061	964	3.23	1335

Altogether, these results suggest that the 150 and 550 J.mm^{-3} specimens are the best according to the *E* and ε criterions, respectively; for the desired application, while the 450 J.mm^{-3} one offering finally the best compromise. In the same time, the 550 J.mm^{-3} specimen exhibited the best chemical homogeneity and then very probably a better corrosion performance. The persistence of a larger number of the Nb/Mo/Ta-rich islands in the 450 J.mm^{-3} specimen compared to the 550 J.mm^{-3} one, might favor pitting corrosion, as a consequence of the (electro)chemical reactivity differences between these islands and the matrix. Also differences between the biological behaviors might be expected between

169 the islands and matrix, when contacted to bone cells. Consequently, to pursue our investigations, a
170 focus was made on the 550 J.mm^{-3} specimen.
171 The electrochemical measurements were thus performed on both 150 and 550 J.mm^{-3} specimens to
172 investigate their corrosion performance. The specimens were exposed to a 0.1 M NaCl (25°C) solution
173 and to a 37°C deoxygenated Dulbecco's Modified Eagle mammal cell culture medium (DMEM) or
174 DMEM supplemented with 20% of fetal bovine serum (FBS) (experimental details in the
175 supplementary data). After ~ 24 h of exposure, their potentiodynamic polarization curves and
176 impedance plots were recorded (Figs. 4(a, b) and 3S(a-d)). Each open circuit potential (OCP) value,
177 given in the inset of the figures is the average potential of at least three electrodes, before being
178 polarized. The corrosion potential (E_{corr}), as well as the corrosion current density (I_{corr}) values for each
179 coupon in each electrolyte are given in these figures. Along with the potentiodynamic polarization
180 curves, some selected SEM images of the pits nucleated during the polarization of the coupons in the
181 DMEM and NaCl electrolytes can be seen in Figs. 4(a) and 3S(b). (more images can be found in Fig.
182 4S).
183 Interestingly, the anodic branches of all the curves (Figs. 4(a) and 3S(b)) exhibited the generation of a
184 large oxidation current, especially in ~ +0.7 V/SHE. This indicates that by polarizing the coupons
185 towards more positive potentials, a considerable degree of dissolution occurs on their surfaces. The
186 OCP of the 550 J.mm^{-3} alloy in the NaCl ($pH_{(25°C)}$ = 6.55) and DMEM + FBS ($pH_{(25°)}$ = 7.70) solutions
187 is the most positive (+0.150 V/SHE). This potential in the DMEM ($pH_{(25°C)}$ = 7.70) solution changes to
188 -0.035 V/SHE. The curves in Fig. 4(a) also depict that although the I_{corr} recorded in the NaCl solution
189 is slightly larger than those of the DMEM and DMEM + FBS solutions, the alloy generated a smaller
190 oxidation current in this solution, compared to the two others.
191 The recorded Nyquist plots of the 550 J.mm^{-3} coupons, show that the resistivity of the alloy in the
192 three solutions is in the order DMEM + FBS > DMEM > NaCl. This can be seen in the polarization
193 resistance and imaginary impedance values in Fig. 4(b). The plot recorded in the NaCl solution has an
194 incomplete/deformed semi-circle which can be fitted with an electrical circuit model based on a
195 constant phase element (*CPE*), parallel to a charge transfer resistance (R_{ct}) element; both in series with
196 a solution resistivity (R_s) element. In DMEM, the recorded plot consists of only a deformed semi-

197 infinite Warburg linear diffusion impedance, that is represented with a Warburg element (*W*) in series
198 with a R_s (Fig. 4(b)). Here it should be noted that the slope of a classic Warburg plot is 45° and plots
199 with degrees > 45° indicate the existence of a greater mass transport limitation. In DMEM + FBS, the
200 recorded plot has an incomplete/deformed semi-circle in the high frequency region, followed with a
201 linear diffusion Warburg impedance, which can be modelled with an electrical circuit based on a *W*
202 element in series with a R_{ct} and parallel to a *CPE*.
203 Comparing the Bode total impedance ($|Z|$) versus frequency plots of the two alloy coupons in the
204 three electrolytes (Fig. 3S(a, d)) allows evidencing that the $|Z|$ of the 550 J.mm^{-3} coupon at the
205 minimum applied frequency is the maximum and minimum for the DMEM and NaCl solutions,
206 respectively. While, in the case of the 150 J.mm^{-3} coupon the largest and smallest minimum frequency
207 $|Z|$ belongs to the plots recorded in the DMEM and DMEM + FBS.
208 To resume the overall electrochemical results, it is clear that the 550 J.mm^{-3} alloy, has a better
209 resistivity to corrosion compared to the 150 J.mm^{-3} alloy, especially in the DMEM and DMEM + FBS
210 media, at least for the 24 h of exposure, which is useful for the desired application.

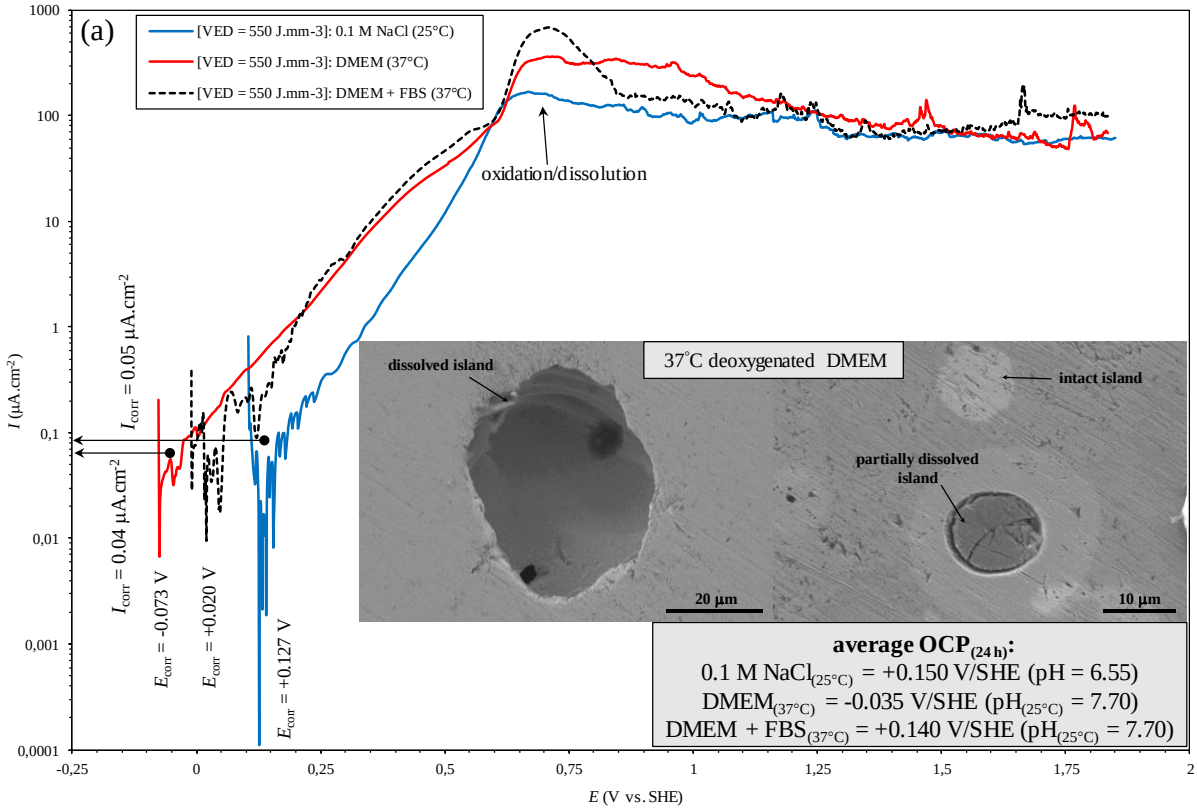

211

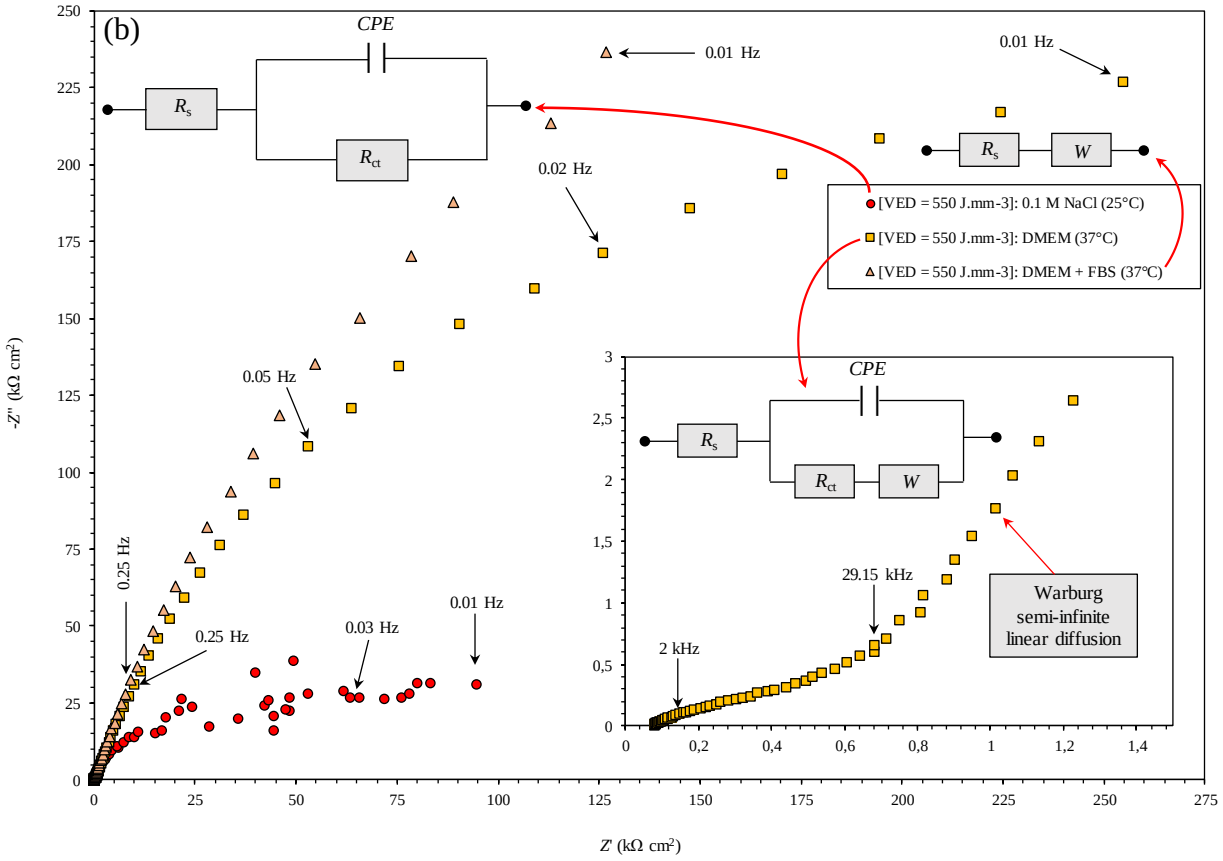

212

213 **FIG. 4.** (a) Potentiodynamic polarization curves and (b) Nyquist plots of the 550 J.mm^{-3} alloy (in the
214 OXY plane), recorded after 24 h exposure to a 0.1 M NaCl (25°C), a deoxygenated DMEM (37°C) and

a deoxygenated DMEM + FBS (80:20 (v/v)) (37°C) media. Inset: SEM images of the pits, nucleated during the polarization of the alloy in DMEM.

Finally, the toxicity of the 550 J.mm^{-3} alloy was evaluated by studying the cell proliferation and morphology in the alloy conditioned and normal media. The conditioned media were prepared by immersing a freshly prepared 550 J.mm^{-3} coupon for 24 h in a 10 mL DMEM-F_{12} medium.

Cells were thus stained (their nucleus and actin cytoskeleton in yellow and purple, respectively) (the experimental details in the supplementary data) and optical images were collected and compared (Fig. 5). The images in Fig. 5 revealed no morphological differences between the cells cultured in the control medium compared to those cultured in the medium conditioned by the alloy. This was consistent with the study of the cell proliferation over 48 h. The number of the viable cells is nearly identical between the cell populations, regardless of whether they were exposed to the conditioned medium or not.

These observations are a strong indication of no acute toxicity of the alloy, suggesting its biocompatibility.

Since it is commonly accepted that the cell proliferation performance gets enhanced by modification of the surface morphology,[17,18] the effect of the surface microstructure, in term of roughness, will be further investigated. Application of the bioactive peptide coatings is also currently under investigation to improve the cell viability, adhesion and proliferation.[19] Up to now, only nude coupons were tested. Here despite the lack of the surface optimization, the biological preliminary results supported the choice of the elaborated alloy as an implant material.

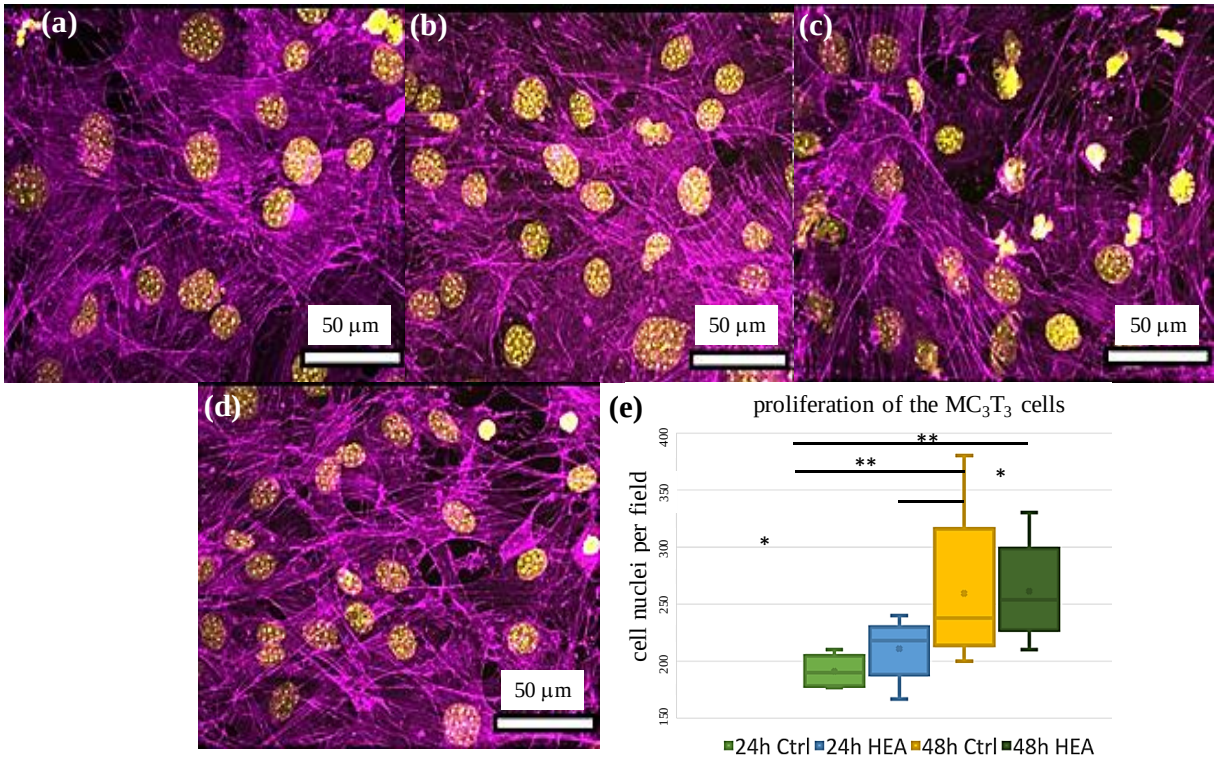

FIG. 5. Optical microscopic images of the MC_3T_3 A A pre-osteoblasts cells cultured in the nonconditioned ((a) 24 h, (b) 48 h) and conditioned media ((c) 24 h, (d) 48 h) and (e) the proliferation graphic (the line within the box represents the median). ANOVA test results: n = 3, * $p < 0.05$, ** $p < 0.01$.

In summary, the L-PBF processed $Ti_{35}Nb_{30}Zr_{29}Mo_3Ta_3$ alloys were investigated, optimizing the elaboration parameters, mainly VED, to tentatively reach a valuable microstructure, mechanical properties, electrochemical corrosion parameters and a biological compatibility toward mammal osteoblast cell proliferation, for a successful integration as bone bioimplants.

Increasing the VED induced the Nb/Mo/Ta solubilization, improving the chemical homogeneity of the processed alloys. Besides, the alloys had a high ability to get plastically deformed. They also exhibited nominal strains of >> 70%, Young modulus values much lower than those of the conventional implant alloys, elastic strains close to those of bones and yield stresses from 900 to 1350 MPa, that increased with increasing the VED, proving the capability of the alloy to be used as a bioimplant material. Focusing on the specimens processed at high VED, their OCPs in the NaCl and DMEM + FBS media were found to be more positive, compared to DMEM, while the impedance parameters of the alloy were much more desirable in contact with the DMEM and DMEM + FBS. Finally, the same

specimen, did not induce acute toxicity and did not inhibit cell proliferation, proving its biocompatibility, supporting their valuability as an implant material.

Supplementary Material

The supplementary data includes the detailed information about the elaboration process, microstructure/mechanical characterization, electrochemical corrosion performance and cytotoxicity behavior of the synthesized alloys.

Acknowledgements

This research was carried out in the framework of The "CoCoA-Bio" (*ANR-20-CE08-0032*) project funded by *Agence Nationale de la Recherche* (ANR). and the CY Initiative (grant "Investissements d'avenir" ANR-16-IDEX-0008).

Author Contributions

Equal: conceptualization, Equal: data curation, formal analysis, writing original draft and project administration.

Data Availability

The data that support the findings of this study are available within the letter and its supplementary material.

REFERENCES

1. K. Prasad, O. Bazaka, M. Chua, M. Rochford, L. Fedrick, J. Spoor, R. Symes, M. Tieppo, C. Collins, A. Cao, D. Markwell, K. (Ken) Ostrikov, K. Bazaka, "Metallic biomaterials: current challenges and opportunities", Materials 10, 884 (2017).
2. United Nations, Department of Economic and Social Affairs, Population Division, "World population prospects Highlights", (2019).

3. D. B. Miracle, O. N. Senkov, “A critical review of high entropy alloys and related concepts”, Acta Mater. 122, 448–511 (2017).
4. J. R. Scully, S. B. Inman, A. Y. Gerard, C. D. Taylor, W. Windl, D. K. Schreiber, P. Lu, J. E. Saal, G. S. Frankel, “Controlling the corrosion resistance of multi-principal element alloys”, Scr. Mater. 188, 96–101 (2020).
5. T. G. De Oliveira, D. V. Fagundes, P. Capellato, D. Sachs, A. A. A. P. Da Silva, “A review of biomaterials based on high-entropy alloys”, Metals 12, 1940 (2022).
6. S. L. Sing, C. F. Tey, J. H. K. Tan, S. Huang, W. Y. Yeong, “3D printing of metals in rapid prototyping of biomaterials: techniques in additive manufacturing, in: Rapid Prototyping of Biomaterials”, Elsevier, pp. 17–40 (2020).
7. J. Feng, D. Wei, P. Zhang, Z. Yu, C. Liu, W. Lu, K. Wang, H. Yan, L. Zhang, L. Wang, “Preparation of TiNbTaZrMo high-entropy alloy with tunable Young’s modulus by selective laser melting”, J. Manuf. Process. 85, 160–165 (2023).
8. S. F. S. Shirazi, S. Gharehkhani, M. Mehrali, H. Yarmand, H. S. C. Metselaar, N. Adib Kadri, N. A. A. Osman, “A review on powder-based additive manufacturing for tissue engineering: selective laser sintering and inkjet 3D printing”, STAM, 16, 033502 (2015).
9. W. Zhang, A. Chabok, B. J. Kooi, Y. Pei, “Additive manufactured high entropy alloys: a review of the microstructure and properties”, Mater. Des. 220, 110875 (2022).
10. C. Liu, Y. Wang, Y. Zhang, L. -C. Zhang, L. Wang, “Deformation mechanisms of additively manufactured TiNbTaZrMo refractory high-entropy alloy: The role of cellular structure”, Int. J Plast. 173, 103884 (2024).
11. W. Li, Y. Huang, Z. Xie, H. Chen, W. Li, B. Liu, B. Wang, “Mechanical property and cellular structure of an additive manufactured $FeCoNiCrMo_{0.2}$ high-entropy alloy at high-velocity deformation”, J. Mater. Sci. Technol. 139, 156–166 (2023).
12. S. Mooraj, J. Dong, K. Y. Xie, W. Chen, “Formation of printing defects and their effects on mechanical properties of additively manufactured metal alloys”, J. Appl. Phys. 132, 225108 (2022).
13. M. Long, H. J. Rack, “Titanium alloys in total joint replacement–a materials science perspective”, Biomater. 19, 1621–1639 (1998).

14. X. Wang, S. Xu, S. Zhou, W. Xu, M. Leary, P. Choong, M. Qian, M. Brandt, Y. M. Xie, "Topological design and additive manufacturing of porous metals for bone scaffolds and orthopaedic implants: a review", Biomater. 83, 127–141 (2016).
15. X. Tong, Q. Sun, D. Zhang, K. Wang, Y. Dai, Z. Shi, Y. Li, M. Dargusch, S. Huang, J. Ma, C. Wen, J. Lin, "Impact of scandium on mechanical properties, corrosion behavior, friction and wear performance, and cytotoxicity of a β-type Ti–24Nb–38Zr–2Mo alloy for orthopedic applications", Acta Biomater. 134, 791–803 (2021).
16. Z. Li, W. Lai, B. Wang, X. Tong, D. You, W. Li, X. Wang, "A novel $Ti_{42.5}Zr_{42.5}Nb_5Ta_{10}$ multi-principal element alloy with excellent properties for biomedical applications", Intermetallics 151, 107731 (2022).
17. H. -T. Lee, C. -C. Lin. "Enhanced cell proliferation on biomedical titanium surfaces by laser ablation-induced micro- and nanoscale hybrid structures", Mater. Trans. 60, 1799–1806 (2019).
18. A. Sumayli, Recent trends on bioimplant materials: A review", Mater. Today Proc. 46, 2726–2731 (2021).
19. H. Ahirwar, Y. Zhou, C. Mahapatra, S. Ramakrishna, P. Kumar, H. Sekhar Nanda, "Materials for orthopedic bioimplants: modulating degradation and surface modification", Coatings, 10, 264 (2020).